



Optical frequency domain reflectometry shape sensing using an extruded optical fiber triplet for intra-arterial guidance

JACYNTHE FRANCOEUR,^{1,*} ANTHONY ROBERGE,² PIERRE LORRE,² FRÉDÉRIC MONET,² CORY WRIGHT,³ SAMUEL KADOURY,⁴ AND RAMAN KASHYAP^{1,2}

¹Department of Electrical Engineering, École Polytechnique Montréal, 2500 Chem. de Polytechnique, Montréal, QC H3T 1J4, Canada

²Department of Physics Engineering, École Polytechnique Montréal, 2500 Chem. de Polytechnique, Montréal, QC H3T 1J4, Canada

³Research and Development, Boston Scientific, 4100 Hamline Ave N, Arden Hills, MN 55112, USA

⁴Department of Computer and Software Engineering, École Polytechnique Montréal, 2500 Chem. de Polytechnique, Montréal, QC H3T 1J4, Canada

*jacynthe.francoeur@polymtl.ca

Abstract: Intra-arterial catheter guidance is instrumental to the success of minimally invasive procedures, such as percutaneous transluminal angioplasty. However, traditional device tracking methods, such as electromagnetic or infrared sensors, exhibits drawbacks such as magnetic interference or line of sight requirements. In this work, shape sensing of bends of different curvatures and lengths is demonstrated both asynchronously and in real-time using optical frequency domain reflectometry (OFDR) with a polymer extruded optical fiber triplet with enhanced backscattering properties. Simulations on digital phantoms showed that reconstruction accuracy is of the order of the interrogator's spatial resolution (millimeters) with sensing lengths of less than 1 m and a high SNR.

© 2022 Optica Publishing Group under the terms of the [Optica Open Access Publishing Agreement](#)

1. Introduction

In the field of interventional medicine, shape and position tracking of medical instruments, such as needles, catheters and endoscopes, plays an important role for guidance inside the human body during minimally invasive procedures that impacts their success. For this purpose, optical fiber shape sensors have received increased interest over the past years for the numerous advantages they offer over other current approaches. For example, fluoroscopy, a widely used X-ray imaging technique for real-time monitoring of surgical instruments, presents drawbacks such as a high cost, bulkiness, a low-speed data acquisition and a concerning patient exposure to radiation [1]. In addition to this, electromagnetic tracking is often sensitive to metallic environments such as in the operating room, making it unusable when sensors are near critical equipment. Optical fiber shape sensors are a competitive alternative to traditional device tracking methods as such since they offer advantages compatible with the essential features required for minimal invasive surgery: intrinsic safety, biocompatibility, embedding capability, flexibility, compactness, light weight and small dimensions [2]. An immunity from electromagnetic interference and a multiplexing capability are other notable advantages of this technology, since it means the sensors may be simultaneously used with magnetic resonance imaging (MRI) [3], and require a single remote interrogation unit [1].

Fiber optic shape sensors are fabricated using either optical multicore fibers or multiple optical single-core fibers. The second alternative offers a wider range of usable optical fibers than the first one and provides higher strain sensitivity thanks to larger spacing of the fiber cores (see Eq. (2)

and Fig. S1 in the Supplementary Material) [4], but often requires complex and costly assembly [1]. The sensor's three-dimensional shape is reconstructed by extracting curvature amplitude and orientation from measuring and comparing the local longitudinal strain in each core along the entire length of the sensor. Beam theory indicates that three distinct strain measurement points, each measured by a different fiber, are sufficient to reconstruct the sensor's 3D shape [3]. Strain can be sensed using different approaches, the most popular being fiber Bragg gratings (FBGs) [5], and Rayleigh scatter [6]. An FBG is a periodic variation in the refractive index of the core of an optical fiber resulting from its exposure to laser radiation in the UV wavelengths or with femtoseconds pulses [7]. The resulting grating structure acts as a wavelength selective mirror for light propagating through the fiber. The reflected wavelength, or Bragg wavelength, is directly proportional to the grating period, which changes when the fiber undergoes mechanical or temperature related stress. Therefore, strain can be measured by tracking the shift of the Bragg wavelength peak. Although FBGs provide a high signal to noise ratio and thus a high strain sensing accuracy, the number of sensing points along the fiber is limited to avoid hindering device efficiency. Therefore a spatial interpolation is required to approximate the strain between sensing points, potentially missing critical variations [8]. Rayleigh scatter originates from inhomogeneities in the refractive index of the fiber core, whose positions change under stress and lead to a shift in the reflection spectrum of the fiber. However, the strength of the Rayleigh signal of standard optical fiber is very weak, resulting in a poor SNR, but can be enhanced, namely by ultraviolet laser exposition [9], nanoparticle-doping [10], or the addition of a continuous uniform [11,12] or random [13] grating. Optical frequency domain reflectometry (OFDR) is a method that interrogates an optical fiber with a frequency swept laser and converts its frequency response into the time/spatial domain by Fourier transform of the backscattered signal arising from any of the afore mentioned scatter enhancement schemes. OFDR enables fully distributed strain sensing along the entire length of the sensor at a fast acquisition speed and with spatial resolutions in the order of millimeters [6].

Surgical equipment navigation has been investigated with fiber optic shape sensors of different features, length (generally from a few centimeters to tens of centimeter) and interrogation approach [1]. This technology finds applications in numerous medical fields, such as ophthalmic [10], colonoscopic [14], and endovascular [15,16] interventions as well as biopsies [17]. For example, a 118 mm long sensor of multicore fibers embedded with FBGs for flexible medical instruments shape sensing purposes was designed by Khan et al. and reached a maximum reconstruction error of 1.05 mm and a maximum mean error of 0.44 mm [14]. Jäckle et al. presented an FBG-based shape sensing approach using a 38 cm long multicore fiber and reached an average error of 0.35–1.15 mm and a maximal error of 0.75–7.53 mm depending on reconstructed shape complexity [16]. A 115 mm long multiple single-core fibers shape sensor containing FBGs was developed by Moon et al. for minimally invasive procedures and reconstructed shapes with a 3.74 Hz refresh rate and with a tip position error of 1.50% of the total sensing length [18]. Westbrook et al. inscribed a continuous chirped FBG in a multicore optical fiber and reconstructed 2D circular shapes over 20 cm using OFDR with an average curvature radius error between 0 mm and 1.1 mm [11]. A distributed shape-sensing device for epidural needle guidance based on OFDR and multiple single-core nanoparticle-doped fibers was assessed by Amantayeva et al. and returned results with errors of ~1% over 7 cm [19]. Megens et al. studied the shape sensing accuracy of Philips Fiber Optic RealShape (FORS) system, a thin multicore fiber inscribed with uniform FBGs, when used within and without a guidewire for 2D and 3D shapes over sensing lengths of 0.5 m to 1.8 m [20]. With a spatial resolution of less than 50 μm , they demonstrated submillimeter shape sensing accuracy, and Herwaarden et al. demonstrated the practicability of the device for endovascular navigation in a human clinical study [21]. Finally, we previously demonstrated a distributed shape tracking system based on OFDR and UV-exposed fibers for intra-arterial guidance that yielded mean errors of 2.8 ± 0.9 mm over a 20 cm catheter

length [15]. Although the characteristics of fiber optic shape sensors for medical applications and their accuracy assessment are extremely variable, the shape sensing accuracy in literature is usually of the millimeter order ($\sim 1\%$ of the total sensing length).

In this context, we present in this work an OFDR grating-based fiber optic shape sensor which can serve as a medical tool for long surgical instruments such as catheters. The shape sensor is composed of three polyimide coated SMF28 equivalent fibers in equilateral cross-sectional arrangement following an extrusion process into a polyethylene and polypropylene copolymer [22]. Using multiple fibers in the triplet has the principal advantage over multi-core fibers of allowing the relative positions of the fiber cores to be controlled at the polymer extrusion stage to tailor the fiber's sensitivity to bending for the intended application. The backscatter power in each fiber contained in the triplet is enhanced by inscribing randomly chirped FBGs through the polyimide coating using a femtosecond laser plane-by-plane direct-writing scheme [7]. With this device, shape sensing of bends of different curvatures and lengths is investigated and demonstrated in both 2D and 3D, in post-processing and in real-time with a minimal refresh rate of 7 Hz.

Advancements with respect to the previous work presented in [23] were made in terms of sensor fabrication, assembly and calibration and more complex shapes were reconstructed over longer sensing lengths (30-40 cm instead of 10-20 cm) and tested in real-time. First, gratings were inscribed directly in polyimide coated fibers using a femtosecond laser writing process instead of using UV exposure that requires the removal of the polymer coating, rendering the bare fibre to become fragile and prone to breaking. Polyimide's high melting temperature ensured the integrity of the fiber coating during the extrusion process. Next, the three fibers were bonded through a polymer extrusion process instead of using UV curing glue, which resulted in a completely flexible and robust sensor with a uniform outer diameter. This method allows longer samples to be assembled and stable equilateral arrangement of the fibers along the entire sensor's length, which leads to calibration with fewer steps. There is indeed no need to rotate the sensor around its axis to measure and evaluate the phase difference between sinusoidal strain variations of the three fibers, as presented in [23]. This also means that calibration can be more easily performed over long lengths.

2. Methods

2.1. Shape sensing principle

The strain measurements used for the shape reconstruction of the sensor were performed by OFDR, as described by Froggatt et al. [6]. An Optical Vector Analyzer (OVA 5000, Luna[©]) was used for the asynchronous shape reconstruction of the sensor (processing and assessment of the strain data from the reference and the sample not performed at the same time as their acquisition) at a spatial resolution of 1.6 mm. The OFDR data processing up to the cross-correlation between the sample and reference spectra was performed by the OVA interrogator. As for real-time shape tracking of the triplet, a fiber optic sensing unit (Sensuron Summit, TSSC[©]) was used, with a spatial resolution of 3.2 mm and a 30 Hz acquisition rate. With the OVA, measurements with much smaller spatial resolution (min. 20 μ m (OVA) versus 1.6 mm (Summit)) can be obtained; however, the Summit exhibits strain signals with a smaller noise amplitude ($\sim 10 \mu$ strain (Summit) versus $\sim 30 \mu$ strain (OVA)), and is capable of real-time measurements (~ 30 Hz (Summit) versus 1 Hz (OVA)) on all three fibers at the same time without the need of additional hardware (4 channels (Summit) versus 1 channel (OVA)) and may be used with longer sensing lengths (max. 13 m (Summit) versus 64 cm (OVA))).

OFDR is an interferometric technique that performs strain measurements as follows. A tunable laser source interrogates the fiber across a bandwidth $\Delta\lambda$ and the backscatter signal is detected in the frequency domain. The signal is transferred to the spatial domain by a Fourier transform to evaluate reflectivity as a function of position along the fiber. The spatial resolution of the system

is determined by the gauge length Δx , which defines the section of the signal centered at the sensing point (or “strain gauge”) x_i across which an inverse Fourier transform is performed to return it to the spectral domain. Then, the frequency response of the sample under strain is cross correlated with a reference (unstrained) measurement taken separately, before taking the sample measurement, resulting in a peak whose position gives the spectral shift for the sensing point x_i . Since this shift is proportional to both temperature and strain changes between the reference and the sample measurements, local strain/temperature can be determined using Eq. (1), where λ_B is the local Bragg wavelength and κ_e and κ_T are strain (ϵ) and temperature (T) constants [8]:

$$\frac{\Delta\lambda_B}{\lambda_B} = \kappa_e \Delta\epsilon + \kappa_T \Delta T \quad (1)$$

This operation is repeated for all sensing points in the sensor, resulting in distributed strain measurements. Figure 1 depicts the working principle of OFDR. Although enabling distributed sensing with fiber optic sensors, OFDR involves trade-offs with regard to sensing range, spatial resolution, acquisition speed and sensitivity [24,25]. For a given frequency sweep range, the sweep period restricts the maximum range achievable in order to be able to discriminate the backscatter signals coming from different sweep periods during acquisition. This issue leads to a trade-off between sensing range and spatial resolution, since a better spatial resolution comes from higher sweep repetition rate, but the latter decreases the sweep period and thus shortens the maximum range. Moreover, at one point in the OFDR pipeline, the signals in the spatial domain are scanned by a sliding window, whose length defines the spatial resolution. The length of the sliding window involves a trade-off between spatial resolution and sensitivity, since increasing the size of the sliding window worsens the spatial resolution but improves sensitivity by processing more data points. Finally, acquisition time with OFDR approximately equals the sweep period. Therefore, reducing its frequency sweep range shortens acquisition time, but also leads to a narrower strain measurement range.

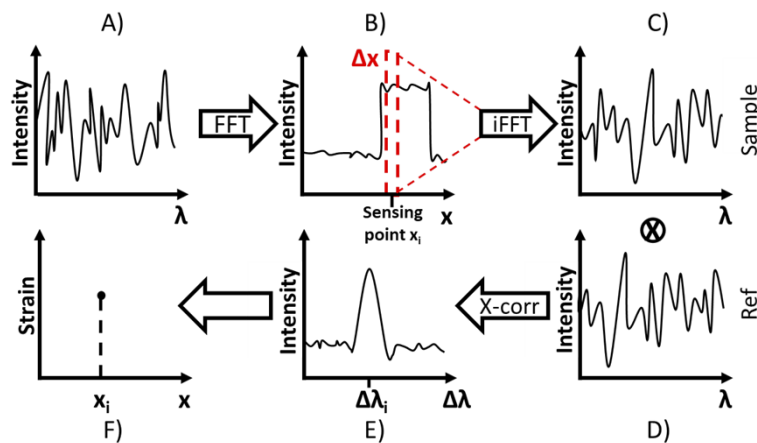


Fig. 1. OFDR data processing steps illustration. A) Frequency response of the fiber under test. B) A Fourier transform is performed to obtain the signal in the spatial domain. C) An inverse Fourier transform is performed across a section Δx of the signal centered at the sensing point x_i to obtain the frequency response of this specific region. D) The local sample (strained fiber) frequency response is cross correlated with the corresponding reference (unstrained fiber) signal. E) The result is a peak centered at spectral shift value for x_i . F) This peak is correlated to the strain applied to the fiber.

Once the distributed strain values along each fiber are evaluated, a geometrical model for the cross-section and segments of the sensor delimited by the spatial resolution Δx , similar to the

one presented by Froggatt et al. [26], is employed to determine the 3D spatial coordinates of the sensor in the tracking frame (Fig. 2). By combining the definition of strain (ratio of the change in length to the length of the fiber) with the expressions for the radii of curvature for each core, the strain equations for the three fibers can be obtained (Eq. (2)) and expressed in terms of local curvature radius (r) and orientation (α) (see [26] for detailed derivation of the equations). Using the geometrical parameters of the extruded triplet, i.e. the distance between the triplet center and each fiber core (a) and the transverse angular position of the three fibers ($\varphi_1, \varphi_{12}, \varphi_{23}$), and the strain measured by the three fibers ($\varepsilon_1, \varepsilon_2, \varepsilon_3$), r and α are estimated by solving the system of nonlinear equations Eq. (3) for each segment of the sensor.

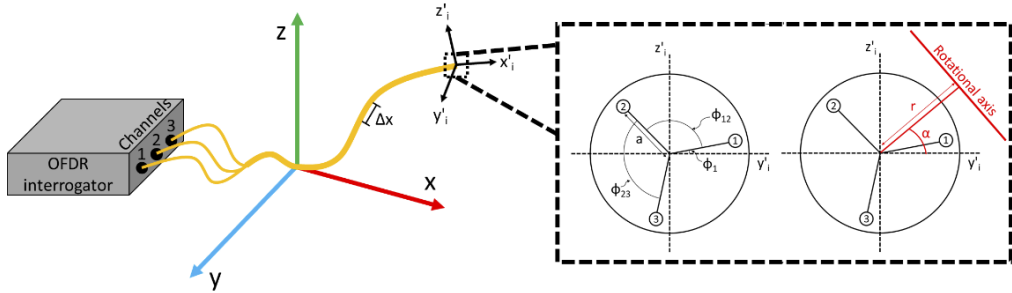


Fig. 2. Experimental setup and geometrical model for shape determination, adapted from [26]. φ_1 is the transverse angular position of fiber 1, φ_{12} is the angle separating fiber 1 and fiber 2 and φ_{23} is the angle separating fiber 2 and fiber 3. α and r are the curvature orientation and radius, respectively, and a is the distance between the triplet center and each fiber core. (x'_i, y'_i, z'_i) defines the coordinate system of the segment of the sensor, whereas (x, y, z) defines the tracking frame.

$$\begin{aligned}\varepsilon_1 &= -\frac{a \cos(\varphi_1 - \alpha)}{r} + \varepsilon_0 \\ \varepsilon_2 &= -\frac{a \cos(\varphi_1 + \varphi_{12} - \alpha)}{r} + \varepsilon_0 \\ \varepsilon_3 &= -\frac{a \cos(\varphi_1 + \varphi_{12} + \varphi_{23} - \alpha)}{r} + \varepsilon_0\end{aligned}\quad (2)$$

$$\begin{aligned}\varepsilon_{12} &= \varepsilon_1 - \varepsilon_2 \\ \varepsilon_{13} &= \varepsilon_1 - \varepsilon_3 \\ \varepsilon_{23} &= \varepsilon_2 - \varepsilon_3\end{aligned}\quad (3)$$

Equation (3) is solved by subtracting two of its three equations, which takes out the curvature radius and leaves only the curvature orientation, that can then be determined by finding the zeros of the remaining function. Subsequently, the curvature radius is determined by using the now known curvature orientation in one of the three equations of Eq. (3). The coordinates of the tip of the segment in its own frame (x'_i, y'_i, z'_i) are derived from these two values (r and α). Successive projections using rotation matrices are then computed to switch from local coordinate systems to a common coordinate system (x, y, z) and reconstruct the 3D shape of the sensor. Since OFDR is sensitive to both temperature and strain, assuming that the three fibers undergo the same temperature fluctuations at a specific sensing location, the offset caused by temperature on the strain measurements (ε_0) is cancelled by solving the equations of the strain differences between the fibers (see Table S1 in the Supplementary Material). Similarly, axial strain is also cancelled (see Fig. S2 in the Supplementary Material).

2.2. Sensor fabrication

Polyimide coated SMF28 equivalent fibers from Fibercore (SM1250(10.4/125)P) were chosen for the fabrication of the sensor. Since the three polyimide coated fibers (155 μm diameter each) fitted nearly perfectly in the tip of the extrusion head, the fibers were secured in the targeted equilateral arrangement along the entire length of the sensor and thus the relative positions between the fibers remained invariant. In addition, the triplet's position with regard to the sensor's neutral axis was seemingly kept uniform along the sensor's length by analyzing cross-sections (see Fig. S3 in the Supplementary Material). Furthermore, polyimide's high melting temperature ensures the coating's integrity during extrusion. By avoiding the need to strip the coating, the fibers are not as fragile and therefore less prone to breaking during the fabrication process and during sensor handling. The fibers were extruded using a twin-screw extruder from Leistritz with a copolymer of polyethylene and polypropylene from TOTAL (M6823MZ). The copolymer was chosen for its fluidity, allowing a coating thickness around the triplet below 200 μm in order to fit in a surgical catheter, and its flexibility, allowing strain to be fully transmitted to the fibers without allowing slippage within. The melting point of the copolymer also allowed extrusion at low temperatures, thereby avoiding the FBGs from being affected. The extrusion process is covered in [22], and a depiction of the extruded triplet is shown in Fig. 3.

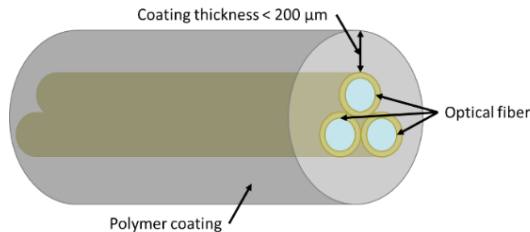


Fig. 3. Triplet schematic.

Prior to extrusion, randomly chirped FBGs were inscribed through the polyimide coating of the three fibers to improve their backscatter signal over 1.5 m. In a chirped FBG, the periodicity of the refractive index modulation varies along the length of the grating, as opposed to a uniform FBG, where the periodicity is constant. Thus, the bandwidth of the spectral response of a chirped FBG is broader than a uniform FBG. Since different wavelengths are reflected by different portions of the grating along its axis, a chirped FBG has a lower insertion loss than a uniform FBG, which allows for longer sensing range. To reduce insertion loss, ultra-weak uniform FBGs rather than standard uniform FBGs can be used, but this leads to weaker backscatter signal and thus poorer SNR. We believe a chirped FBG is therefore advantageous compared to an ultra-weak FBG without a chirp. The femtosecond laser plane-by-plane direct-writing scheme used, that allowed the inscription through the coating, is described in [7]. Hence, one by one, the fibers were mounted on a high precision 1 m long 1D translation stage and a 1030 nm Pharos laser (250 fs pulse, tunable repetition rate) was focused into the fiber core by a microscope objective. The position of each refractive index modification was controlled by synchronizing the motion of the stages with each laser pulse. The gratings inscription was monitored with an optical backscatter reflectometer (OBR 4600, Luna \circledR). The gratings were inscribed with a slowly varying random chirp, to obtain a random spectral response that exhibit a primary wavelength centered around 1540 nm, but that has a bandwidth broader than uniform period FBGs.

2.3. Calibration

Because of the different fiber lengths between the sensing region of each fiber and the interrogator, the distributed sensing points of the three fibers in the triplet are misaligned. Heat induced strain

peaks were used as references to align the sensing points of the three fibers together before the shape reconstruction steps.

Since the fibers were free to rotate transversally during the extrusion process, an additional calibration step was taken to characterize the fibers' random angular positions along the triplet's length and to fine-tune the strain constant in Eq. (1), which was critical to accurately perform shape sensing. To do so, a non-destructive approach was devised, consisting of extracting the strain constant and the fibers' position at each sensing point using the measured strain signals of the sensor in a reference shape. This method was simple, fast and adapted for both short and long lengths. Calibration amounted to reversing the shape reconstruction process. The latter uses the arrangement of the fibers within the triplet ($\varphi_1, \varphi_{12}, \varphi_{23}, a$) (see Fig. 2) and the strain measured by each of them ($\varepsilon_1, \varepsilon_2, \varepsilon_3$) to deduce the local angular offset (α) and curvature radius (r) by solving Eq. (3). Conversely, the strain constant and the fiber positions (φ_1 , since φ_{12} and φ_{23} are constant) can be determined by putting the sensor into a specific shape (known α and r , e.g. a circle using a cylinder) and measuring the resulting strain signals. Because of the different spatial resolutions and sensing lengths, calibration had to be performed with both the OVA (asynchronous sensing) and the Summit (real-time sensing) prior to the reconstructions. The results were averaged over six calibrations around a 21 cm diameter cylinder for most asynchronous reconstructions and performed once around a 16.4 cm diameter cylinder before measurements for the real-time reconstructions. For the asynchronous reconstruction of a 2D sine wave, the sensor was calibrated beforehand using the sine wave for reference, and the results were averaged over four calibrations. The validity of the calibration approach was assessed by characterizing a fiber bundle from TSSC[®] with a 1.5 cm period constant twist (Fig. 4(A)). Calibration was performed on the fabricated sensor inserted in a 0.038" guidewire compatible catheter from Terumo[®] and fixed at both ends with shrink tubes to minimize displacement inside the catheter. Figure 4(B) shows the fiber positions returned by the six calibrations around the 21 cm diameter cylinder. The strain constant of those calibrations averaged to 1.016 strain⁻¹.

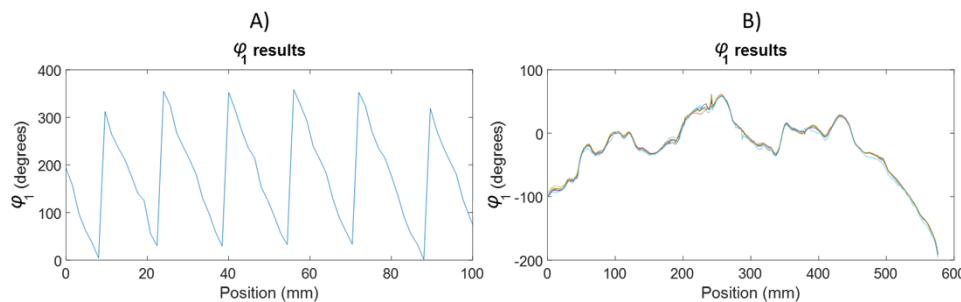


Fig. 4. A) Calibration validation. This plot shows that the calibration procedure accurately recovered the 1.5 cm period constant twist of a fiber bundle from TSSC[®]. B) Calibration results around a 21 cm diameter cylinder.

2.4. Simulations

Several shape sensing simulations were performed to investigate the effect of the length of the triplet sensor, noise level, spatial resolution (Fig. 5(A) and (B)) and shape complexity on average reconstruction accuracy (defined as the Euclidean distance between corresponding points on the real and simulated shapes). For each input value of these experimental parameters, the results were averaged over 50 simulations and the standard deviation was evaluated. When one parameter was varied, the others were fixed to the following values: 3.2 mm spatial resolution (spatial resolution used with the Summit), 10 μ strain noise amplitude (approximate noise amplitude in a random FBG fiber with the Summit), 800 mm sensing length (full catheter length) and

simple shape. The simulations were carried out as follows. First, a random shape was created by generating random values of curvature radius (r) and orientation (α) over the entire sensor's length at a spatial resolution much smaller than the experimental one (0.1 mm). The shape complexity was adjusted to better mimic a real shape by filtering the generated random values. Then, the values were resampled at the experimental spatial resolution and converted to strain distributed in the three fibers using Eq. (2). An independent noise value was added to mimic an experimental measurement. This simulated experimental strain data was then converted back to curvature radius and angle offset values using Eq. (3) and the shape was reconstructed, which was compared to the original, higher-resolution and noise-free shape. A sensor with straight fibers (constant φ_1) was used to simplify the simulations. To evaluate the effect of shape complexity on the average position error of the sensor, irregular shapes were simulated by reducing initial data filtering and by reducing the minimal local curvature radius. The impact of sensing length and spatial resolution on processing speed was also evaluated by continuously generating simulated strain data and processing it as it would be experimentally using a workstation.

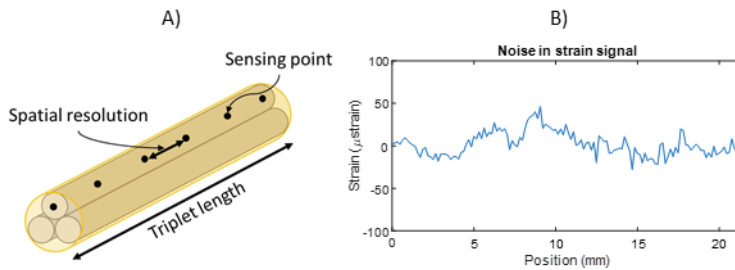


Fig. 5. Shape sensing experimental parameters. A) Triplet length and spatial resolution. B) Example of typical noise in strain signal of a section in one fiber, measured with the OVA.

2.5. Shape reconstruction

Once the strain constant was adjusted and the arrangement of the fibers in the triplet was determined over the entire region of interest of the sensor through calibration, 2D and 3D shape tracking was performed, both in real-time and asynchronously to evaluate the accuracy of the method. For the latter, three shapes were printed on millimetric sheet, and the sensor was placed upon the shape and fixed to the printed shape. One shape was a 32.5 cm long exponential curve, another was a 20.6 cm long half-sine curve, and the last was a 40 cm long sine curve. In addition to planar shape reconstruction, the half-sine curve was wrapped around a 15.6 cm diameter cylinder to assess shape reconstruction in three dimensions. Considerable precautions were taken to minimize sensor torsion by reconstructing over lengths smaller than 50 cm and by reconstructing the sensor attached to a template. The error was calculated by comparing the reconstructed shape with the theoretical shape after registration. This process was repeated eight to twelve times for each shape. The real-time shape tracking was performed over a 22.4 cm catheter segment inserted in different branches of a lung model.

3. Results and discussion

3.1. Sensor fabrication

Figure 6(A) and (B) show the backscatter amplitudes and spectra of the three fibers after laser writing measured with the OBR. Although the alignment procedure was optimized to compensate for the inhomogeneous thickness of the polyimide coating, scattering amplitude fluctuations over fiber length can be seen. Indeed, local alignment over such a large length (1.5 m) to maintain the uniformity of the backscattering signal is a challenging task. Therefore, sensing instruments

with a large dynamic range were required to avoid dead zones in the sensor. The fabrication process resulted in gratings with backscatter level 40 dB higher than fiber unexposed to the laser, significantly reducing strain noise level. A drop in signal around two thirds of the length can be seen in the time domain plot of one fiber since the translation stage had a limited length of 1 m and thus the 1.5 m grating inscription had to be performed in two steps (1 m, then 0.5 m). Slight differences in the frequency spectra of the three gratings can be also noted, one being stretched over a larger bandwidth, despite inscribing the same chirp profile in all three fibers. This can be explained by the fibers slipping between the stage clamps because of their polyimide coating, reducing the tension applied and thus changing the period and the Bragg wavelength of the gratings. The scanning bandwidth during shape sensing was adjusted to cater for these differences and thus the performance of the sensor was not affected.

Following the laser writing, the three fibers were brought together through an extrusion process in a copolymer. While the current sensor grating is currently only 1.5 meters long, the extrusion process has no intrinsic limitation of length, and can make sensors of hundreds of meters in length, with the production of longer random gratings, as recently demonstrated [27]. A cross-section microscopic image of the resulting triplet with the important geometrical parameters for shape sensing is shown in Fig. 6(C). The final device had a diameter of approximately 600 μm and could reach a 2.3 cm curvature radius without breaking or the fibers slipping within the polymer (see Fig. S4 in the Supplementary Material). Since, following a robust extrusion process, the relative positions between the fibers and the spacing of the cores to the neutral axis were assumed constant along the sensor's length, slight variations of these parameters could have contributed to mismatches between the real and reconstructed shapes. Additional steps to the calibration method would help to fully account for possible slight variations of these parameters, for example by rotating the bent sensor around its axis to measure and evaluate the phase difference between sinusoidal strain variations of the three fibers and their amplitude at every sensing point, similarly to the approach presented in [23], but would involve more measurement, especially over long lengths.

3.2. Simulations

Simulation results are displayed in Fig. 7. All results show the same trend, which is that average reconstruction accuracy increases when processing a shorter sensing length, strain signals with a lower noise level, a smaller spatial resolution and a reduced complexity of shape (an average of (3.1 ± 0.4) mm for a simple shape, versus an average of (3.9 ± 1.2) mm for a complex shape). The shape reconstruction process, which is performed iteratively segment by segment, starting at the base of the sensor, is one main causes of reconstruction inaccuracy, since the position error of a segment is transmitted to the next, increasing the error on the position of the latter, and so on until the triplet is fully reconstructed. Therefore, larger position errors result from reconstructing over longer lengths and with an increased local error, that can be caused by larger spatial resolution, higher noise level or increased curvature (more complex shape). Overall, the simulated results show that average reconstruction accuracy is of the order of the interrogator's spatial resolution (3.2 mm in the simulations) with sensing lengths of less than 1 m and a high SNR (30 μstrain or less). In a medical setting, working with smaller spatial resolutions is preferable to reach an accuracy closer to 1 mm, and ultimately submillimeter errors are sought.

As for processing speed, using a workstation to perform shape sensing, it is best to process shorter sensing lengths and larger spatial resolutions. The simulations returned a minimal refresh rate of 7 Hz for processing strain data, which is adequate for continuous shape tracking. With a faster GPU, a processing speed of 30 Hz, the data acquisition speed of the Summit interrogator, could be reached for shape tracking of the full catheter length (80 cm) at the smallest spatial resolution of the Summit interrogator (1.6 mm).

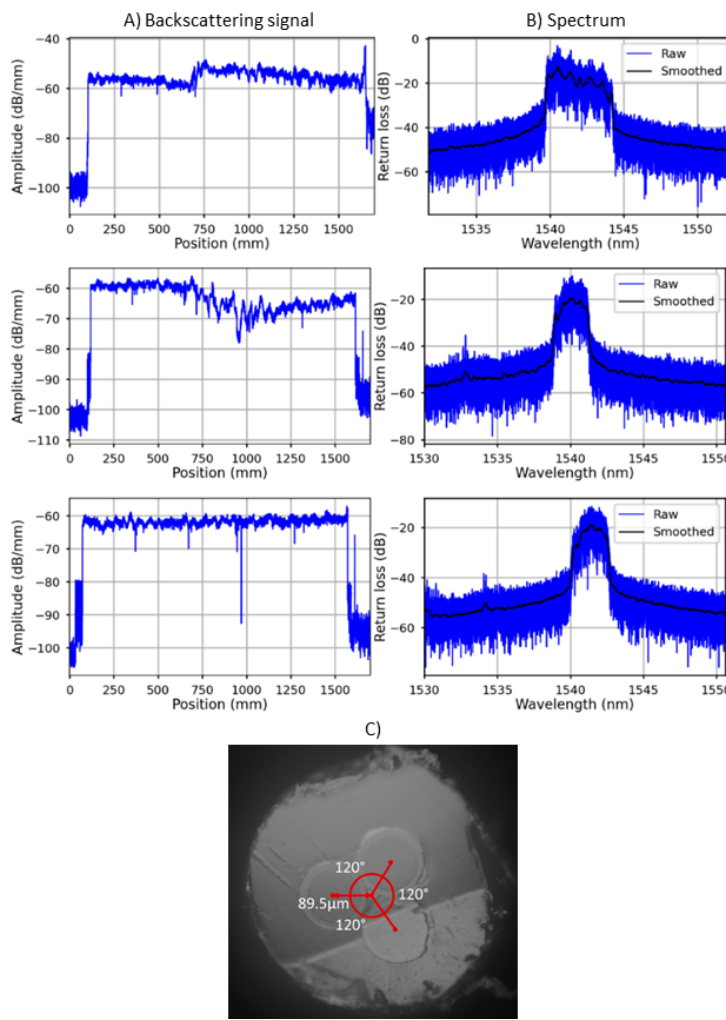


Fig. 6. Backscattering signal of the three fibers in the A) time domain and B) frequency domain. The third time domain plot from the top exhibits a drop in signal amplitude around 1 m that comes from the two steps of grating inscription (1 m translation stage). The reflected wavelengths peaks of the three fibers are centered at 1542 nm, 1540 nm and 1541 nm (top to bottom) and large of 5 nm, 3 nm and 3 nm (top to bottom). C) Triplet cross-section microscopic image, showing angles of 120° separating fibers (equilateral arrangement) and a core-center distance of 89.5 μm .

3.3. Shape reconstruction

Figure 8 shows all asynchronous shape reconstruction results after registration with the theoretical shape. Figure 8(A) and (D) present the results for the 2D and 3D half-sine curve, respectively, Fig. 8(B) presents the results for the 2D sine curve and Fig. 8(C) presents the results for the 2D exponential curve. The position error results (Euclidian distance) are recorded in Table 1. Two main observations can be made from the generated shapes. First, the error on the shorter length reconstructions (e.g. half-sine curve) is smaller than the error on the longer length reconstructions (e.g. exponential curve). Second, the error on the simpler reconstructions (e.g. 2D exponential and half-sine curves) is smaller than the error on the more complex reconstructions (2D sine curve)

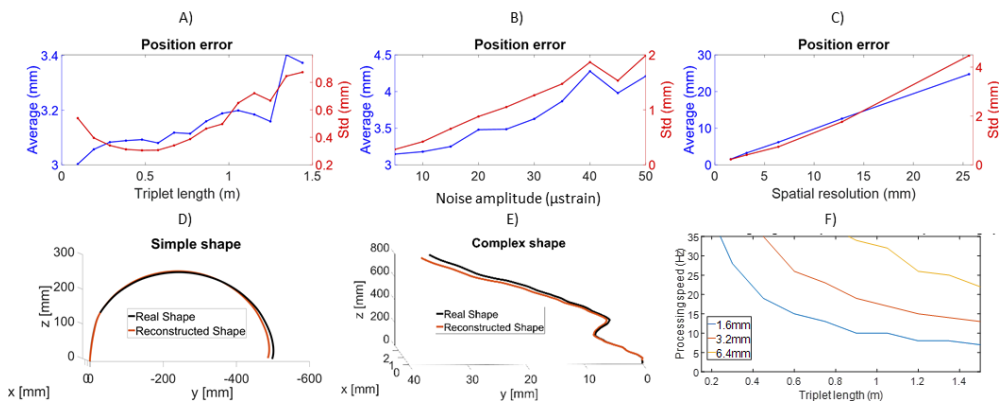


Fig. 7. Simulation results. Effect on average reconstruction accuracy of A) triplet sensing length, B) spatial resolution, C) noise amplitude and D) and E) shape complexity. F) Impact of spatial resolution and sensing length on data processing speed. A minimal refresh rate of 7 Hz is reached with a 1.5 m sensing length and 1.6 mm spatial resolution. Std: Standard deviation.

and 3D half-sine curve). These observations were predicted by the simulations. The mean errors are on average between 0.8 mm and 2.6 mm and thus are of the order of the spatial resolution of the strain signals measured with the OVA (1.6 mm). Literature on medical applications of fiber optic shape sensors presents on average errors of the millimeters scale, or approximately 1% of the shape sensing length [1]. Encouragingly, our results are of the same order of magnitude and for shapes of varying curvature amplitude, both in 2D and 3D, and readily fall within tolerance in a medical setting.

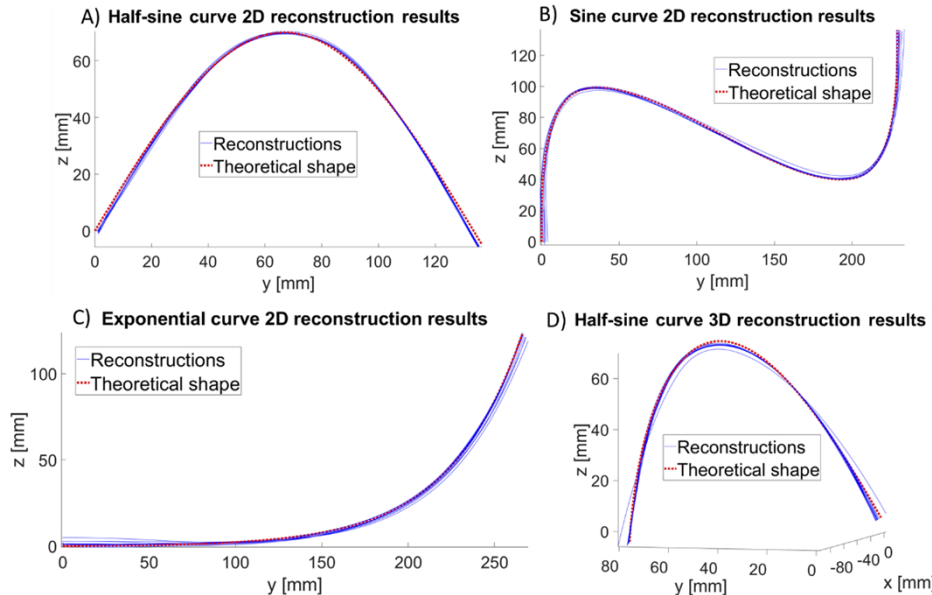


Fig. 8. Asynchronous reconstruction results of A) a 2D half-sine curve, B) a 2D sine curve, C) a 2D exponential curve and D) a 3D half-sine curve. 12 measurements per shape were performed in A), C) and D), whereas 8 were performed in B).

Table 1. Asynchronous reconstructions position errors

| # | Exp 2D (32.5 cm) | | | Half-sine 2D (20.6 cm) | | | Half-sine 3D (20.6 cm) | | | Sine 2D (40 cm) | | |
|-----------|------------------|-----------|-----------|------------------------|------------|------------|------------------------|-----------|-----------|-----------------|-----------|-----------|
| | Mean (mm) | Std (mm) | Max (mm) | Mean (mm) | Std (mm) | Max (mm) | Mean (mm) | Std (mm) | Max (mm) | Mean (mm) | Std (mm) | Max (mm) |
| 1 | 1.8 | 0.5 | 2.6 | 1.2 | 0.5 | 1.6 | 0.7 | 0.3 | 1.1 | 1.2 | 0.3 | 1.7 |
| 2 | 0.9 | 0.4 | 1.4 | 1.0 | 0.5 | 1.7 | 0.9 | 0.3 | 1.3 | 8.4 | 5.1 | 16.9 |
| 3 | 1.9 | 0.8 | 3.0 | 0.6 | 0.3 | 1.2 | 1.5 | 0.7 | 2.5 | 1.0 | 0.3 | 1.5 |
| 4 | 1.4 | 0.5 | 2.1 | 0.5 | 0.3 | 1.3 | 1.2 | 0.4 | 1.9 | 1.8 | 0.9 | 3.2 |
| 5 | 1.2 | 0.5 | 1.9 | 1.1 | 0.4 | 1.6 | 3.7 | 1.9 | 6.0 | 3.1 | 1.1 | 4.9 |
| 6 | 1.2 | 0.4 | 1.8 | 0.8 | 0.4 | 1.4 | 1.5 | 0.6 | 2.1 | 1.3 | 0.5 | 1.8 |
| 7 | 0.7 | 0.2 | 1.1 | 0.9 | 0.4 | 1.7 | 1.3 | 0.7 | 2.2 | 2.0 | 0.8 | 3.4 |
| 8 | 1.9 | 0.9 | 2.7 | 0.8 | 0.3 | 1.5 | 1.5 | 0.5 | 2.1 | 1.6 | 0.8 | 3.1 |
| 9 | 1.5 | 0.4 | 1.9 | 0.6 | 0.3 | 1.2 | 1.3 | 0.7 | 2.3 | - | - | - |
| 10 | 1.0 | 0.5 | 1.7 | 0.8 | 0.3 | 1.2 | 1.6 | 0.8 | 2.6 | - | - | - |
| 11 | 3.1 | 1.4 | 5.0 | 0.7 | 0.3 | 1.3 | 1.4 | 0.4 | 1.8 | - | - | - |
| 12 | 2.2 | 1.0 | 3.2 | 0.7 | 0.3 | 1.1 | 1.5 | 0.7 | 2.5 | | | |
| Mean (mm) | 1.6 | 0.6 | 2.4 | 0.8 | 0.4 | 1.4 | 1.5 | 0.7 | 2.4 | 2.6 | 1.2 | 4.6 |
| (%) | 0.7 | 0.5 | 0.2 | 0.7 | 0.40 | 0.20 | 1.1 | 0.7 | 0.3 | 0.6 | 0.3 | 1.1 |
| | ± 0.6 | ± 0.3 | ± 1.1 | ± 0.2 | ± 0.1 | ± 0.2 | ± 0.7 | ± 0.4 | ± 1.2 | ± 2.4 | ± 1.6 | ± 5.1 |
| | ± 0.3 | ± 0.2 | ± 0.1 | ± 0.1 | ± 0.09 | ± 0.03 | ± 0.6 | ± 0.4 | ± 0.2 | ± 0.6 | ± 0.4 | ± 1.3 |

The full sine curve was accurately reconstructed by calibrating the sensor beforehand using the sine curve for reference. Without this extra step, the additional inflection point couldn't be accurately recovered, potentially because of increased sensor twisting due to the increased shape complexity or because of signal losses induced by the more complex bending. This result demonstrates the need for a torsion compensation strategy for reconstructing more complex shapes without having to calibrate using the intended shape to reconstruct and points towards calibration based off complex shapes (e.g. in 3D instead of 2D and with a varying curvature radius) being helpful for improving reconstruction accuracy in such cases by factoring in what calibration based off simple shapes (e.g. 2D circle) does not.

A capture of real-time shape reconstruction inside a branch of a lung model is shown in Fig. 9. The distance between the extremities of the reconstructed shape with the corresponding dimension on the lung model (measured freehand with a ruler) is shown for quantitative purposes. The overall appearance of the reconstructed shape matches the branch anatomy from the phantom. At the experimental spatial resolution (3.2 mm) and sensing length (22.4 cm), the refresh rate of the 3D plot reached the 30 Hz acquisition rate of the Summit.

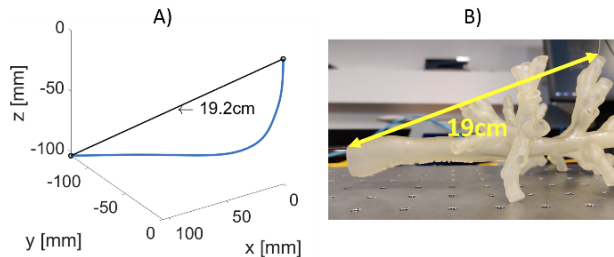


Fig. 9. Rendering of real-time shape reconstruction inside a lung model over a 22.4 cm catheter segment. A) Experimental result and B) real-life shape.

Shape tracking error mostly arises from the drawbacks of the geometrical reconstruction model, noise in the strain signals and torsion of the sensor. Indeed, the error propagation from one reconstructed segment to the next translates into a distortion between the reconstructed shape and the real shape, which increases with sensing length. To lessen error propagation, an approach to try out would be to check if the difference in curvature of two successive segments is within a given threshold, and if not, correct the curvature accordingly [23]. As for the stochastic noise in the strain signals, although a moving average was implemented in the algorithm to smooth the data and improve reconstruction accuracy, further analysis is required to identify its origin and determine approaches for minimization, such as hardware modifications to the experimental setup. Device torsion is a determinant factor of the shape tracking accuracy, since it changes the values of φ_1 from those determined during calibration. Although quite resistant to torsion, the catheter could twist slightly during its shaping and the triplet was free to twist within the catheter since it had not been anchored inside, but only at each extremity. Therefore, a first step to correct the sensor torsion issue would be to glue the triplet to the inner surface of the catheter. Since torsion of the device is inevitable, a torsion compensation strategy would still need to be implemented. The strain generated by twisting being modest due to the proximity of the fibers and their pitch in the sensor [28,29], twisting sensitivity could be increased by adding extra fibers in the device, which is possible with the polymer extrusion approach, and inducing a controlled twist in the triplet as it is extruded [30]. Similar to the work by Ko et al. [31], the twist of the sensor could be determined by comparing the strain measured by the outer cores with the one measured by the inner cores. Also, since the triplet is not fixed inside the catheter, it is very likely that strain is not fully transmitted from the catheter to the fibers, therefore inducing a larger reconstruction error. Gluing the sensor to the catheter would solve this issue. Finally, registration between the fibers is a possible source of reconstruction inaccuracy since the measurement technique consists of holding the ~1 mm wide pointed tip of a soldering iron close to the sensor to locally induce a strain peak from the heat source simultaneously in all three fibers. It is possible that the sensor would register two different perturbation points, but this is highly unlikely as the resolution of the OVA 5000 and Summit are 1.6 mm and 3.2 mm, respectively, much wider than the tip of the soldering iron. A misalignment between sensing points would lead to a mismatch of the strain measurements from the three fibers and thus deviate the calculated curvature radius and orientation from the correct values. In future work, the fibers could be aligned by cutting the triplet towards the end of the gratings and aligning the end of the strain signals. To avoid unwanted reflections at the cut end, one could index match the cut ends. By making all these changes to our measurement method, the achievable accuracy on the sensor position could be additionally increased, and with a smaller spatial resolution (microns), we aim to enhance the shape sensing accuracy of our sensor to less than a millimeter, the same order reported by Megens et al. [20].

4. Conclusion

In summary, three polyimide coated SMF28 equivalent fibers were assembled in a triplet through an extrusion process in a polyethylene-polypropylene copolymer after a femtosecond laser random grating writing process that increased the backscatter of each fiber by 40 dB. The enhanced backscatter signal ensured an improved SNR over inherent Rayleigh scatter and the extrusion approach resulted in a resistant, yet flexible device that had stable fiber positions and could fit inside a surgical catheter. The enhanced signal allows several optical components to be inserted inline without degradation in SNR. The effect of the experimental parameters (sensing length, spatial resolution, noise in the strain signals and shape complexity) on the average reconstruction accuracy was investigated through simulations, which showed that shape sensing works best when decreasing each individual parameter. They also revealed the propagation of the error from one segment to the next during shape reconstruction, the principal drawback from the

geometric model employed. A simple calibration process suited for both long and short lengths was implemented. This geometrical characterization step was facilitated by the stable triplet position along the entire length of the sensor that was ensured by the direct polymer extrusion process developed in our laboratory. Experimental shape tracking was performed asynchronously and in real-time inside the branches of a lung model. Our asynchronous method returned average mean errors of 0.8 mm and 1.6 mm for 2D simple curves of 20.6 cm and 32.5 cm, respectively, of 1.5 mm for a 3D simple curve of 20.6 cm and of 2.6 mm for a 2D complex curve of 40 cm. These results are of the same order of magnitude as most results seen in literature (error of around 1% of the total sensing length) and approach that required in a clinical environment. In addition, shape tracking of a 22.4 cm segment of our designed sensor was demonstrated at a high refresh rate. Future work will investigate calibration using different shapes as well as shape sensing with random FBG fiber triplets of different random phase functions, since the laser-writing process would be faster and more cost-effective [13]. However, this will require more processing steps from the interrogator unit as it would involve the processing of more complex spectral responses. The results of the improvements will be reported in a future publication.

Funding. Boston Scientific Corporation; Canadian Institutes of Health Research; Natural Sciences and Engineering Research Council of Canada (Canada Graduate Scholarships – Master's (CGS M)).

Acknowledgments. Portions of this work were presented at the Optical Sensors topical meeting collocated with the Optical Sensors and Sensing Congress that took place on 11–15 July 2022 in Vancouver, British Columbia, Canada, *Real-time 3D Shape Sensing with a Random Fiber Bragg Grating Triplet* (SM2C.2). R. Kashyap acknowledges the substantial support from the Canadian Foundation for Innovation program for the infrastructure used in this research.

Disclosures. The authors declare no conflicts of interest.

Data availability. Data underlying the results presented in this paper are not publicly available at this time but may be obtained from the authors upon reasonable request.

Supplemental document. See [Supplement 1](#) for supporting content.

References

1. I. Floris, J. M. Adam, P. A. Calderón, and S. Sales, "Fiber Optic Shape Sensors: A comprehensive review," *Opt. Lasers Eng.* **139**, 106508 (2021).
2. B. Lee, "Review of the present status of optical fiber sensors," *Opt. Fiber Technol.* **9**(2), 57–79 (2003).
3. K. Mandal, F. Parent, S. Martel, R. Kashyap, and S. Kadoury, "Vessel-based registration of an optical shape sensing catheter for MR navigation," *Int. J. Comput. Assist. Radiol. Surg.* **11**(6), 1025–1034 (2016).
4. I. Floris, J. Madrigal, S. Sales, P. A. Calderón, and J. M. Adam, "Twisting measurement and compensation of optical shape sensor based on spun multicore fiber," *Mech. Syst. Signal Process.* **140**, 106700 (2020).
5. Sensuron, "Introduction to Fiber Optic Sensing," retrieved <https://www.sensuron.com/introduction-to-fiber-optic-sensing/>.
6. M. Froggatt and J. Moore, "High-spatial-resolution distributed strain measurement in optical fiber with Rayleigh scatter," *Appl. Opt.* **37**(10), 1735–1740 (1998).
7. A. Roberge, S. Loranger, J.-S. Boisvert, F. Monet, and R. Kashyap, "Femtosecond laser direct-writing of high quality first-order Bragg gratings with arbitrary complex apodization by phase modulation," *Opt. Express* **30**(17), 30405–30419 (2022).
8. Sensuron, "Fiber Optic Sensing Fundamentals," retrieved <https://www.sensuron.com/fiber-optics-sensing-fundamentals/>.
9. S. Loranger, M. Gagné, V. Lambin-Iezzi, and R. Kashyap, "Rayleigh scatter based order of magnitude increase in distributed temperature and strain sensing by simple UV exposure of optical fibre," *Sci. Rep.* **5**(1), 11177 (2015).
10. A. Beisenova, A. Issatayeva, I. Iordachita, W. Blanc, C. Molardi, and D. Tosi, "Distributed fiber optics 3D shape sensing by means of high scattering NP-doped fibers simultaneous spatial multiplexing," *Opt. Express* **27**(16), 22074–22087 (2019).
11. P. S. Westbrook, T. Kremp, K. S. Feder, W. Ko, E. M. Monberg, H. Wu, D. A. Simoff, T. F. Taunay, and R. M. Ortiz, "Continuous Multicore Optical Fiber Grating Arrays for Distributed Sensing Applications," *J. Lightwave Technol.* **35**(6), 1248–1252 (2017).
12. R. Duncan and M. Raum, *Characterization of a fiber-optic shape and position sensor*, SPIE Smart Structures and Materials + Nondestructive Evaluation and Health Monitoring (SPIE, 2006), Vol. 6167.
13. F. Monet, S. Loranger, V. Lambin-Iezzi, A. Drouin, S. Kadoury, and R. Kashyap, "The ROGUE: a novel, noise-generated random grating," *Opt. Express* **27**(10), 13895–13909 (2019).
14. F. Khan, A. Denasi, D. Barrera, J. Madrigal, S. Sales, and S. Misra, "Multi-Core Optical Fibers With Bragg Gratings as Shape Sensor for Flexible Medical Instruments," *IEEE Sens. J.* **19**(14), 5878–5884 (2019).

15. F. Parent, M. Gérard, F. Monet, S. Loranger, G. Soulez, R. Kashyap, and S. Kadoury, "Intra-Arterial Image Guidance With Optical Frequency Domain Reflectometry Shape Sensing," *IEEE Trans. Med. Imaging* **38**(2), 482–492 (2019).
16. S. Jäckle, T. Eixmann, H. Schulz-Hildebrandt, G. Hüttmann, and T. Pätz, "Fiber optical shape sensing of flexible instruments for endovascular navigation," *Int. J. Comput. Assist. Radiol. Surg.* **14**(12), 2137–2145 (2019).
17. A. Leibinger, M. J. Oldfield, and F. Rodriguez y Baena, "Minimally disruptive needle insertion: a biologically inspired solution," *Interface Focus* **6**(3), 20150107 (2016).
18. H. Moon, J. Jeong, S. Kang, K. Kim, Y.-W. Song, and J. Kim, "Fiber-Bragg-grating-based ultrathin shape sensors displaying single-channel sweeping for minimally invasive surgery," *Opt. Lasers Eng.* **59**, 50–55 (2014).
19. A. Amantayeva, N. Adilzhanova, A. Issatayeva, W. Blanc, C. Molardi, and D. Tosi, "Fiber Optic Distributed Sensing Network for Shape Sensing-Assisted Epidural Needle Guidance," *Biosensors* **11**(11), 446 (2021).
20. M. Megens, M. D. Leistikow, A. van Dusschoten, M. B. van der Mark, J. J. L. Horikx, E. G. van Putten, and G. W. T. Hooft, "Shape accuracy of fiber optic sensing for medical devices characterized in bench experiments," *Med. Phys.* **48**(7), 3936–3947 (2021).
21. J. A. van Herwaarden, M. M. Jansen, E.-j. P. A. Vonken, T. Bloemert-Tuin, R. W. M. Bullens, G. J. de Borst, and C. E. V. B. Hazenberg, "First in Human Clinical Feasibility Study of Endovascular Navigation with Fiber Optic RealShape (FORS) Technology," *Eur. J. Vasc.* **61**(2), 317–325 (2021).
22. P. Lorre, F. Monet, M. Gauthier, A. Poiffaut, A. Roberge, S. Kadoury, and R. Kashyap, *Extruded complex optical fiber structures for shape sensing and biomedical applications (Conference Presentation)*, SPIE OPTO (SPIE, 2020), Vol. 11283.
23. F. Parent, S. Loranger, K. K. Mandal, V. L. Iezzi, J. Lapointe, J.-S. Boisvert, M. D. Baiad, S. Kadoury, and R. Kashyap, "Enhancement of accuracy in shape sensing of surgical needles using optical frequency domain reflectometry in optical fibers," *Biomed. Opt. Express* **8**(4), 2210–2221 (2017).
24. C. Liang, Q. Bai, M. Yan, Y. Wang, H. Zhang, and B. Jin, "A Comprehensive Study of Optical Frequency Domain Reflectometry," *IEEE Access* **9**, 41647–41668 (2021).
25. S. Zhao, J. Cui, L. Suo, Z. Wu, D.-P. Zhou, and J. Tan, "Performance Investigation of OFDR Sensing System With a Wide Strain Measurement Range," *J. Lightwave Technol.* **37**(15), 3721–3727 (2019).
26. M. E. Froggett and R. G. Duncan, "Fiber optic position and/or shape sensing based on rayleigh scatter," US2008212082 (4 September 2008).
27. F. Monet, A. Roberge, and R. Kashyap, "Physical Unclonable Functions based on random gratings," in *Latin America Optics and Photonics (LAOP) Conference 2022*, Technical Digest Series (Optica Publishing Group, 2022), Th1A.5.
28. I. Floris, J. Madrigal, S. Sales, P. Calderón, and J. Adam, *Twisting compensation of optical multicore fiber shape sensors for flexible medical instruments*, SPIE BiOS (SPIE 2020), Vol. 11233.
29. R. Xu, A. Yurkewich, and R. V. Patel, "Curvature, Torsion, and Force Sensing in Continuum Robots Using Helically Wrapped FBG Sensors," *IEEE Robot. Autom. Lett.* **1**(2), 1052–1059 (2016).
30. P. Westbrook, K. Feder, T. Kremp, T. Taunay, E. Monberg, J. Kelliher, R. Ortiz, K. Bradley, K. Abedin, D. Au, and G. Puc, *Integrated optical fiber shape sensor modules based on twisted multicore fiber grating arrays*, SPIE BiOS (SPIE, 2014), Vol. 8938.
31. W. Ko, K. S. Feder, X. Sun, J. Li, and P. S. Westbrook, "Simultaneous interrogation of multiple cores in a shape sensor fiber with a graded index fiber micro-turnaround," *Opt. Express* **30**(14), 24452–24460 (2022).